
Mechanistic Interpretability of Graph Motifs via Sparse Autoencoders on Graph Neural Networks

Shervin Goudarzi, Harry Huang, Manhar Gupta

Department of EECS

University of California, Berkeley

Berkeley, CA

Abstract

Graph neural networks excel at learning from graph-structured data, yet whether their internal representations align with known topological motifs remains unclear. We apply sparse autoencoders to decompose GNN hidden activations trained on synthetic graphs with ground-truth motif annotations, including feedback loops, cascades, and fan-out structures. Using point-biserial correlation with rigorous permutation testing, we discover that GNNs spontaneously learn monosemantic features corresponding to specific graph motifs. Critically, this interpretability is architecture-dependent: Graph Convolutional Networks develop highly localized, motif-specific features requiring minimal sparsity, while Graph Attention Networks distribute motif information across significantly more features. Causal ablation experiments confirm that identified features are functionally necessary and removing feedback loop features selectively degrades performance only on graphs containing those structures. Interestingly, single input module motifs were also causally linked to feedback loops, suggesting that these two motifs might not be mutually exclusive. Our results reveal a fundamental trade-off in graph neural architectures: fixed message-passing operators compress topological patterns into interpretable circuits that uses and identifies graphical topology for output prediction, even without explicit training using motif labels. This work establishes that mechanistic interpretability of graph representations is achievable and demonstrates that architectural and topological inductive biases critically determine the structure of learned topological encodings.

1 Introduction and Background

Graphical motifs structures within the context of GNNs have not been studied in depth when determining a model's performance on masked node prediction. Certain graphical motifs, that have a relation to biological contexts, are important to consider when understanding the underlying activations of a GNN. These directed networks or "motifs" as we will call them in this manuscript encode the causal logic, such as feedforward loops, feedback cycles, and cascades, that governs key patterns in science, including biology. In recent years, Graph Neural Networks (GNNs) have emerged as the dominant paradigm for modeling such relational data. The mathematical foundation for efficient learning on graph structures was formalized by Kipf and Welling [1] with the Graph Convolutional Network (GCN), which enables models to aggregate local neighborhood information effectively. Fout et al. [2] demonstrated the power of these architectures in computational biology, specifically for protein interface prediction, proving that GNNs can learn complex, biologically relevant spatial relationships.

Since these foundational works, GNNs have been applied to increasingly complex problems. Zitnik

et al. [3] utilized GNNs to model polypharmacy side effects, capturing higher-order interactions between drugs and protein targets that simple pairwise models missed. To address the heterogeneity of graphs, Veličković et al. [4] introduced Graph Attention Networks (GATs), which allow nodes to learn dynamic weighting schemes for their neighbors, potentially improving model expressivity on irregular regulatory networks. However, as the predictive power of these models has grown, so has their opacity. While GNNs can predict molecular outcomes with high accuracy, understanding *how* they reason about the underlying topology remains a significant challenge. Dwivedi et al. [5] highlighted this gap, proposing standardized benchmarks for GNN interpretability, yet most existing methods rely on post-hoc feature importance measures rather than decomposing the model's internal representations.

Parallel to these developments in graph learning, the field of mechanistic interpretability has made strides in deciphering the internal states of Large Language Models (LLMs). Bricken et al. [6] provided a theoretical framework for "monosemanticity," arguing that neural networks often encode multiple concepts in single neurons (polysemanticity), which obscures interpretation. They proposed dictionary learning via Sparse Autoencoders (SAEs) as a method to disentangle these superimposed concepts into sparse, interpretable features. Cunningham et al. [7] successfully applied this technique to finding highly interpretable features in language models, effectively "opening the black box" of transformer activations. More recently, Templeton et al. [8] demonstrated that this approach scales to massive frontier models like Claude 3 Sonnet, extracting millions of interpretable features that abstract away from individual neurons.

The intersection of these fields, GNN and SAE-based interpretability, remains largely unexplored. A notable exception is the recent work by Garcia and Ansuini [9], who applied sparse autoencoders to Protein Language Models, identifying interpretable structural and functional features within sequence-based representations. However, many of the real world problems are not just sequence based; it is fundamentally about *networks*. To date, no systematic study has applied SAEs to understand how GNNs internalize the discrete topological motifs. This project bridges this gap. By training GNNs on simulated topological motifs with ground-truth motif structures and analyzing their activations via SAEs, we aim to determine if the "computational primitives" learned by the GNN align with the structural motifs that are currently known to science.

2 Methodology

The methodology implemented in this study follows a comprehensive multi-stage pipeline designed to rigorously evaluate the interpretability of graph neural networks. The process begins with the generation of synthetic, motif-annotated graphs, proceeds to the training of a Graph Neural Network (GNN) for node-level imputation, involves the learning of Sparse Autoencoders (SAEs) on frozen intermediate activations, and concludes with a statistical evaluation of interpretability through motif correlation and causal ablation.

2.1 Virtual Data Construction and Simulation

The foundation of our dataset is a collection of 4,000 directed weighted graphs generated via a custom stochastic block model framework. These graphs are stored as pickled NetworkX objects, with filenames encoding their underlying structural logic. Specifically, graph IDs are partitioned by motif type: IDs 0–999 represent feedforward loops, 1000–1999 represent feedback loops, 2000–2999 represent single input modules (SIM), and 3000–3999 represent linear cascades.

We simulated node-level "expression" dynamics on each graph. We evolved these states over 50 discrete time steps using a noisy, leaky dynamical system defined by the update rule:

$$x_{t+1} = (1 - \gamma)x_t + \gamma\sigma(Wx_t) + \epsilon_t \quad (1)$$

Here, the leak rate γ was set to 0.3, and σ represents a sigmoid nonlinearity clipped to a finite range

to prevent numerical instability. The noise term ε_t was drawn from a zero-mean Gaussian distribution with a standard deviation of 0.01. The nodes were initialized from a random uniform distribution [-1, 1] and each graph will have precisely 10 nodes; number of motif types per graph could vary. The final state vector at $t = 50$ was treated as the ground truth expression y . To justify our choice for $t = 50$ and standard deviation of 0.01, we conducted data sensitivity analysis by testing the GCN and GAT models at fixed hyperparameters with varied simulation dynamics (different timesteps and different noise levels) in Section 3.2

To validate the simulation duration, we analyzed expression dynamics across all motifs. As shown in Figure 1, different topologies exhibit distinct convergence characteristics.

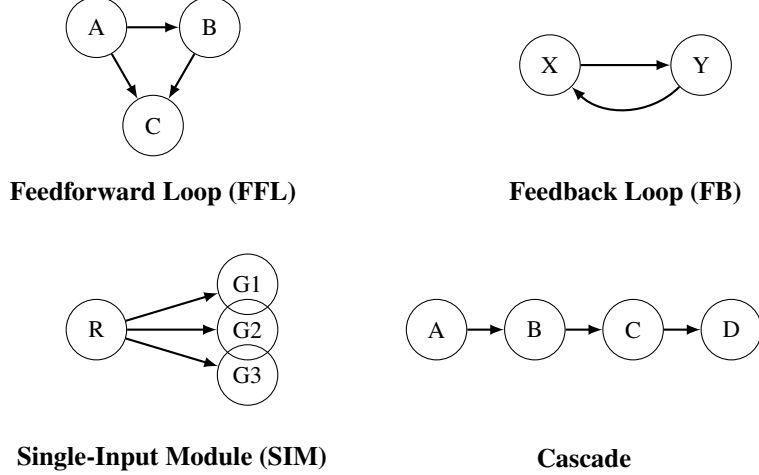


Figure 1: Canonical graph motifs used for synthetic data generation. Each motif represents a distinct regulatory pattern: Feedforward Loop ($A \rightarrow B \rightarrow C$ with $A \rightarrow C$), Feedback Loop (mutual regulation between X and Y), Single-Input Module (one regulator controlling many genes), and Cascade (sequential activation chain).

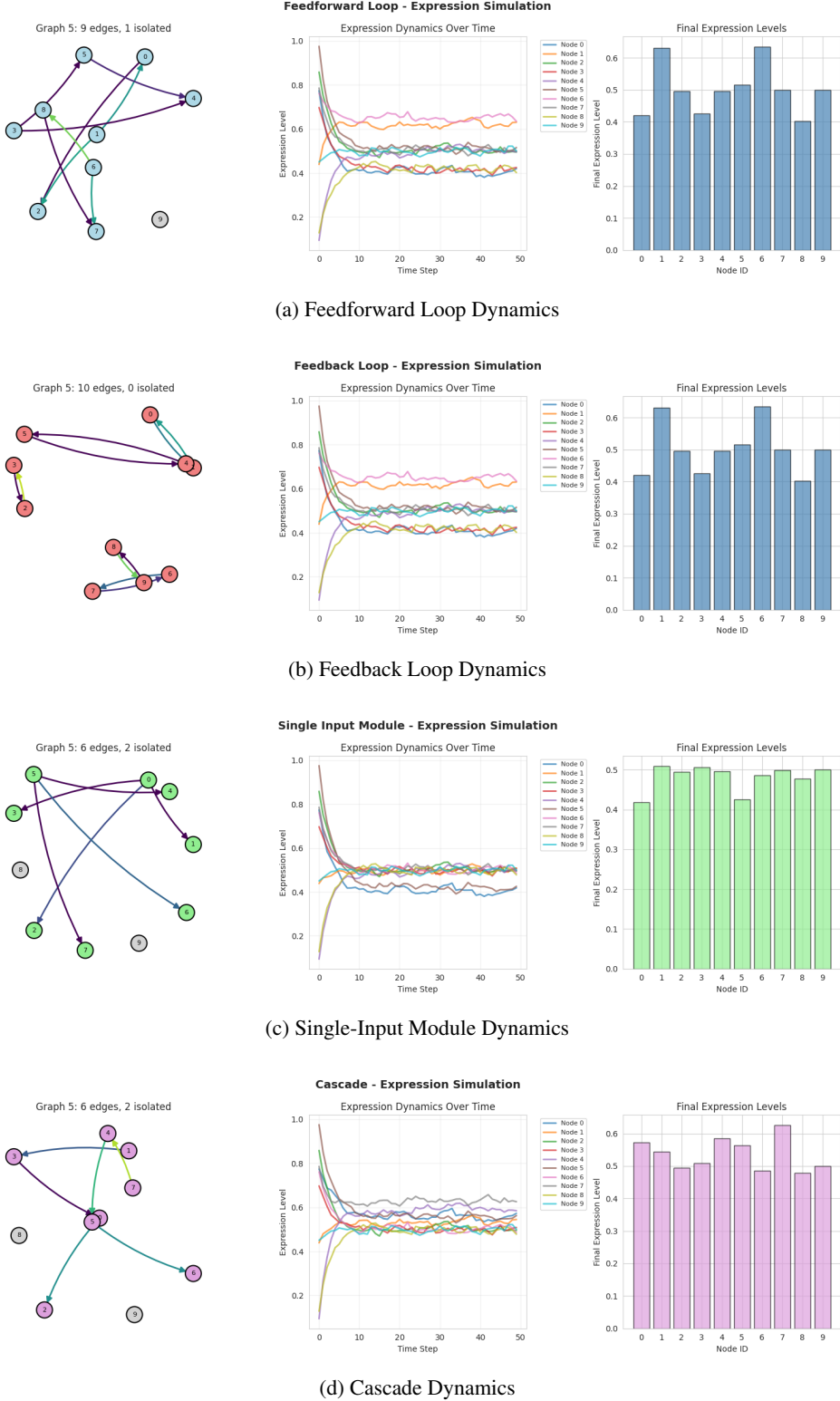


Figure 2: Simulation of expression dynamics across the four primary motif types. The left panels show the specific graph instantiation with edge weights. The center panels track the node values over 50 time steps, showing how different topologies lead to different convergence behaviors. The right panels show the final stable states used for training.

2.2 Graph Neural Network Training

The prediction task was framed as an inductive imputation problem. For each graph, nodes were randomly masked with a probability of $p = 0.2$. The input features provided to the GNN consisted of two channels per node: the first channel contained the expression value (set to zero if masked, and otherwise normalized by the maximum expression in the graph), and the second channel was a binary indicator variable (1 if observed, 0 if masked).

The training process utilized a standard 80/10/10 split (Train/Validation/Test) for the graphs. To prevent overfitting, we employed an early stopping mechanism with a patience of 25 epochs. Hyperparameter optimization was conducted via a distributed, multi-GPU sweep using the Optuna framework, searching over hidden dimensions, dropout rates, and learning rates.

2.2.1 Graph Convolutional Network (GCN)

The primary architecture evaluated was a three-layer Graph Convolutional Network (GCN). To handle the directed, weighted nature of the regulatory interactions without imposing incorrect assumptions about graph laplacians, we employed graph convolutions without symmetric normalization. For a layer l with input node features $H^{(l)}$ and weighted adjacency A , the propagation rule is given by:

$$H^{(l+1)} = \text{ReLU} \left(\text{Dropout} \left(AH^{(l)} W^{(l)} + b^{(l)} \right) \right) \quad (2)$$

where $W^{(l)}$ and $b^{(l)}$ are the learnable weight matrix and bias vector. The network maps dimensions $2 \rightarrow 88 \rightarrow 64 \rightarrow 1$. The 64-dimensional bottleneck $H^{(2)}$ serves as the embedding space for the SAE analysis. The objective function was the Mean Squared Error (MSE) computed strictly on the set of masked nodes \mathcal{M} :

$$\mathcal{L}_{\text{GNN}} = \frac{1}{|\mathcal{M}|} \sum_{i \in \mathcal{M}} (y_i - \hat{y}_i)^2 \quad (3)$$

2.2.2 Graph Attention Network (GAT)

We also trained a three-layer Graph Attention Network (GAT) with the same reconstruction objective. Unlike the GCN, which relies on fixed adjacency multiplications, the GAT assigns learnable importance weights to each incoming edge. For layer l , with K_l attention heads, the propagation rule is

$$H_i^{(l+1)} = \text{ELU} \left(\left\| \sum_{k=1}^{K_l} \alpha_{ij}^{(l,k)} W^{(l,k)} H_j^{(l)} \right\| \right), \quad (4)$$

where the attention coefficients

$$\alpha_{ij}^{(l,k)} = \text{softmax}_j \left(\text{LeakyReLU} \left(a^{(l,k)\top} [W^{(l,k)} H_i^{(l)} \| W^{(l,k)} H_j^{(l)} \| e_{ij}] \right) \right)$$

depend on the learned vector $a^{(l,k)}$ and the explicit edge feature e_{ij} (the original interaction weight). To align with the SAE analysis, the network uses the dimension flow $2 \rightarrow 64 \rightarrow 64 \rightarrow 1$: the first layer has 2 heads of size 32, the second layer fixes 8 heads of size 8 (yielding the 64-dimensional representation consumed by the SAE), and the final layer is a single-head attention that produces scalar predictions. Dropout of 0.0 is applied after each attention block. The loss mirrors the GCN case, namely Mean Squared Error over the masked node set \mathcal{M} , and the model is trained for 200 epochs with patience set to 25 so that the full schedule is executed.

2.2.3 Performance Variance Across Seeds.

To rigorously quantify the performance differences between GNN models and baselines, we employ a multi-seed statistical framework that addresses reproducibility concerns common in machine learning research. Each model (GCN, GAT, MLP, Mean baseline) is trained independently across $N = 20$ random seeds, with each seed controlling weight initialization, data shuffling, and node masking patterns. For each seed $s \in \text{range}\{20\}$, we record the test set MSE computed exclusively on masked nodes. The mean, median, P25, P75, interquartile range (IQR), standard deviation, 95% CI, min and max across test loss of the model runs across the listed seeds has been reported. Results obtained from these multi-seed runs are used subsequently for doing pairwise correlation tests to compare graph-based methods (GCN and GAT) with non-graph/baseline methods (MLP).

2.2.4 Baseline Models for Comparative Evaluation

To establish the value of graph-structured learning and validate that the GNN architectures capture motif-specific patterns beyond simple feature-based prediction, we implemented one baseline model:

Fixed architecture of GCN and GAT for baseline comparison During baseline comparison analysis, we froze the architecture to $2 \rightarrow 128 \rightarrow 64 \rightarrow 1$ for GCN and $2 \rightarrow 32 \times 4 = 128 \rightarrow 8 \times 8 = 64 \rightarrow 1$ where the second layer configuration is based on what was reported for intermediate GAT layers in the foundational GAT paper (Veličković et al. [4]). The first layer has been fixed at 128 for the GCN similar to standard intuition in deep learning where we begin with projecting inputs to a higher dimensional space and progressively reduce in dimension to get more meaningful features. Intermediate layers 32×4 for the first layer of GAT gets us the same amount of features (128) as in GCN. For getting to the second layer with lower hidden dim than 32, 8 made sense as it matches the configuration in the original GAT paper (Veličković et al. [4]) and also allows us to increase the number of heads, allowing the network to learn more varied representations in the second layer.

MLP Baseline (Feature-Only Learning) To isolate the contribution of graph structure, we implemented a multi-layer perceptron (MLP) that operates exclusively on node features without access to the graph topology. The MLP architecture mirrors the depth of the GNN models: $2 \rightarrow 128 \rightarrow 64 \rightarrow 1$, with ReLU activations and dropout (0.2) applied after each hidden layer. The input consists of the same two-channel node features used by the GNNs: normalized expression and mask indicator.

2.2.5 Statistical Evaluation of Baseline Performance

Because model performance across random seeds is heteroscedastic, often non-Gaussian, and derived from paired evaluations on identical data splits, we adopt a fully nonparametric analysis. We use the **Wilcoxon signed-rank test** to assess whether paired differences between model variants are statistically significant without assuming normality. To quantify the magnitude and direction of these differences, we report the **rank-biserial correlation effect size** as the corresponding effect size associated with Wilcoxon. For rank-biserial effect size, we provide **95% bootstrapped confidence intervals**, which offer assumption-free uncertainty estimates and remain valid under skewed or heavy-tailed performance distributions. This combination yields a robust and reproducible assessment of performance differences under stochastic training.

Wilcoxon Signed-Rank Test. For each comparison, we apply the Wilcoxon signed-rank test, a non-parametric paired test that makes no assumptions about the distribution of performance differences. The test operates on the paired differences $\delta_s = \text{MSE}_s^{(A)} - \text{MSE}_s^{(B)}$ for models A and B trained with the same seed s . The null hypothesis H_0 is that the median difference is zero (i.e., the two models

perform equivalently). We reject H_0 at significance level $\alpha = 0.05$ if the two-tailed p-value falls below this threshold.

Rank-Biserial Correlation Effect Size. Statistical significance alone does not indicate practical importance. To quantify the magnitude of performance differences, we compute the rank-biserial correlation coefficient r_{rb} , which is defined as:

$$r_{rb} = 1 - \frac{2U}{n_1 n_2} \quad (5)$$

where U is the Mann-Whitney U statistic (equivalent to the Wilcoxon statistic for paired data after appropriate transformation), and $n_1 = n_2 = 20$ is the number of seeds. The coefficient $r_{rb} \in [-1, 1]$ measures the effect size, with the following interpretation:

- $|r_{rb}| < 0.1$: Negligible effect
- $0.1 \leq |r_{rb}| < 0.3$: Small effect
- $0.3 \leq |r_{rb}| < 0.5$: Medium effect
- $|r_{rb}| \geq 0.5$: Large effect

Bootstrap Confidence Intervals. To quantify uncertainty in the effect size estimates, we generate bootstrap confidence intervals via resampling with replacement. For each pairwise comparison, we draw 10,000 bootstrap samples from the original n_1 (number of seeds) performance measurements per model, recompute the effect size for each bootstrap sample, and report the 95% confidence interval as the 2.5th and 97.5th percentiles of the bootstrap distribution. Narrow confidence intervals indicate precise effect estimates, while wide intervals suggest high variability.

This statistical framework allows us to make robust claims about model superiority beyond single-run anecdotal evidence, addressing reproducibility and statistical rigor in deep learning benchmarks.

2.2.6 Hyperparameter Optimization via Optuna

To ensure optimal model performance and facilitate fair comparison across architectures, we conducted systematic hyperparameter optimization using the Optuna framework [10]. Optuna employs a Tree-structured Parzen Estimator (TPE) sampling algorithm, which models the conditional distribution of hyperparameters given the objective value and iteratively samples from regions of the hyperparameter space that are likely to yield improved performance.

The optimization was performed independently for each architecture (GCN and GAT) to account for architecture-specific optimal configurations. For each trial, the objective function was defined as the validation loss after training for a maximum of 100 epochs with early stopping (patience = 25). The search space encompassed the following hyperparameters:

- **Learning rate:** Log-uniform distribution in the range $[10^{-5}, 10^{-1}]$
- **Hidden dimensions:**
 - GCN Layer 1 hidden dim (channels): $\{8, 128\}$ with a step of 8
 - GAT heads per layer: $\{2, 4, 6, 8\}$ for layer 1, fixed at 8 for layer 2
 - GAT channels per head: $\{8, 128\}$ with a step of 8 for layer 1, fixed at 8 for layer 2
- **Dropout rate:** Uniform distribution in $[0.0, 0.5]$
- **Batch size:** Fixed at 128

Each hyperparameter optimization study consisted of 20 trials. The best-performing configuration was selected based on the minimum validation loss achieved across all trials. To ensure reproducibility, all trials within a single study used the same data split, (seed = 42), isolating the effect of hyperparameters from data variability.

2.3 Fixed Hyperparameter Choices

Hyperparameter sweep is notably done for learning rate, dropout, hidden dimensions and number of heads (only for GAT). In this section, we report the hyperparameters that are fixed for all/certain experiments and provide concise motivations tied to prior literature. Where possible we adopt values recommended by canonical GNN and masked-autoencoder and sparse-autoencoder studies to ensure reproducibility and fair model comparison.

Batch size. We train all models with `batch_size = 128`. This setting balances gradient noise, GPU throughput, and memory constraints for medium-scale graph representation learning. Prior masked-graph modeling work provides empirical precedent for batch sizes in the 64–256 range: Hou et al. [13] report dataset-specific moderate batch sizes for GraphMAE pretraining, while Li et al. [14] analyze the computational benefits of masked graph modeling that permit larger batches. More recently, the hierarchical masked-graph autoencoder Hi-GMAE explicitly adopts `batch_size = 256` for pretraining (Liu et al. [18]), demonstrating that batches at or above 128 are standard in contemporary GMAE pipelines. Although MISATO does not perform masked-node reconstruction, its molecular GNN baselines are commonly trained with `batch_size = 128` on ligand-level quantum-mechanical regression tasks (Siebenmorgen et al. [11]), providing a domain-proximate precedent that 128 is practical and stable for molecular graph workloads.

Model widths and second-layer size: To make activations comparable between architectures we use a second-layer output dimension of 64 for all models (GCN, GAT) and for the SAE analysis (the output/result after the decoder). For GAT this also allows us to match the original architecture choice (8 heads with 8 features each $\rightarrow 8 \times 8 = 64$) which is the setting reported by the original GAT paper (Veličković et al. [4]). The original GCN paper used smaller hidden sizes for the small citation benchmarks (e.g., 16) [1] but we intentionally increase the GCN output to 64 so that downstream SAE analyses receive embeddings of equal dimension across models (this is a common practice when comparing representational geometry across model families) [1, 12]. In summary, the second layer is fixed throughout all experiments based on architectural choices in foundational literature ([1],[4]). The first intermediate layer is where hyperparameter sweep via Optuna (as in Section 2.2.6) is carried out. Except for multi-seed variance and baseline comparison analysis, all experiments using GNNs or GNN activations are using the optimal hyperparameters obtained from the sweep.

GAT internals (hidden dimensions and heads): We follow the original GAT architectural configuration of 8 attention heads with 8 features per head in our 2nd layer, as reported by Veličković et al. [4]. One thing to note is that the original GAT paper only had one intermediate GAT layer which is where 8×8 configuration was used (while we have two to reach two hop neighborhoods). They motivated this choice through extensive ablation studies on citation networks (Cora, Citeseer, Pubmed), demonstrating that multi-head attention with $K = 8$ heads stabilizes the learning process and allows the model to jointly attend to information from different representation subspaces at different positions in the graph. They found that using 8 features per head strikes an optimal balance between model expressivity and computational efficiency, while the multi-head mechanism provides implicit ensemble learning that improves robustness. For our second layer, this yields $8 \times 8 = 64$ total dimensions, matching our standardized bottleneck for SAE analysis. The original paper reported that increasing the number of heads beyond 8 provided diminishing returns, while fewer heads led to less stable training dynamics on graph-structured data.

Masking probability (`mask_prob`): We use `mask_prob = 0.2`. Masked graph autoencoder work has shown that reconstruction performance and downstream transfer vary with mask ratio and that conservative masking ratios (e.g., 0.1–0.3) are often a stable starting point for discriminative downstream tasks, while larger ratios may be workable but can degrade performance depending on redundancy in node features and graph homophily [13, 14]. We therefore choose 0.2 as a conservative masking rate that provides a meaningful reconstruction task while retaining sufficient observed context for stable SAE learning.

Optimizer, learning rate and training schedule: We use Adam with a baseline learning rate `lr=1e-3` for the baseline comparison analysis. A learning rate of 10^{-3} is a common default in modern GNN work and appears frequently in both empirical GNN studies and GNN AutoML search ranges; it provides a stable baseline for comparisons across architectures (we report experiments with identical optimizer settings for all models). [15, 16].

Epochs and early stopping: We train for up to `num_epochs=100` with early stopping (validation patience = 25). A 100-epoch budget combined with a moderate patience value offers sufficient time for convergence on the medium-scale benchmarks used in this study while avoiding overfitting; patience of 20–50 epochs is common in applied deep learning and has been used in recent GNN / autoencoder papers as a conservative stopping heuristic [17, 13]. We also save the best validation checkpoint and report metrics from that checkpoint.

Concat vs. final projection: The choice to `concat=True` in intermediate attention layers (and `concat=False` in the final layer) follows the original GAT design: concatenation across heads increases representational capacity mid-network, whereas the final layer projects to logits without concatenation for stable classification outputs [4]. When comparing representations we keep this canonical behavior to ensure our GAT baseline mirrors the original design.

Practical notes and reproducibility: For every hyperparameter tuning experiment we fix the random seed (`seed = 42`). Only for multi-seed variance we run each model across multiple seeds (from 0 to 19) and obtain statistical data about test loss from masked nodes. Baseline comparison analysis uses this test loss data to do pairwise tests talked about earlier.

2.4 Sparse Autoencoder Learning

To decompose the GNN’s internal representations, we trained Sparse Autoencoders (SAEs) on the frozen 64-dimensional activations $h \in \mathbb{R}^{64}$ from the second hidden layer. Crucially, the SAEs were trained and validated using activations derived strictly from the same training and validation graphs used to train the GNN. The test graphs were reserved exclusively for inference and downstream interpretability analysis to ensure no data leakage occurred between the dictionary learning and evaluation phases.

The SAE architecture consists of a linear encoder, a sparsity constraint, and a linear decoder. The encoder maps the input to a high-dimensional latent space $z \in \mathbb{R}^L$ via an affine transformation followed by a ReLU activation:

$$z = \text{ReLU}(W_{\text{enc}}h + b_{\text{enc}}) \quad (6)$$

Sparsity is enforced via a "Top-K" mechanism, which retains only the k largest activations and zeros out the rest, effectively setting the majority of the latent units to zero:

$$\tilde{z} = \text{TopK}(z, k) \quad (7)$$

The decoder then reconstructs the input \hat{h} from the sparse latent vector \tilde{z} :

$$\hat{h} = W_{\text{dec}}\tilde{z} + b_{\text{dec}} \quad (8)$$

The model is optimized by minimizing the reconstruction error (Mean Squared Error) over the batch of N node activations:

$$\mathcal{L}_{\text{SAE}} = \frac{1}{N} \sum_{i=1}^N \|h_i - \hat{h}_i\|^2 \quad (9)$$

We performed a comprehensive hyperparameter sweep to identify the optimal configuration, varying the latent dimension $L \in \{128, 256, 512\}$ and the sparsity constraint $k \in \{4, 8, 16, 32\}$.

2.4.1 Hyperparameter Selection via Point-Biserial Correlation

The selection of the optimal SAE configuration was driven by the alignment between learned features and ground-truth biological motifs. We quantified this alignment using the point-biserial correlation coefficient (r_{pb}), which measures the relationship between a continuous variable (latent feature activation) and a binary variable (motif presence). For a given latent feature z and a binary motif indicator m (where $m = 1$ if the node belongs to the motif and 0 otherwise), r_{pb} is calculated as:

$$r_{pb} = \frac{M_1 - M_0}{s_n} \sqrt{\frac{n_1 n_0}{n^2}} \quad (10)$$

where M_1 and M_0 are the mean activations for nodes within and outside the motif, respectively; n_1 and n_0 are the counts of nodes in each group; n is the total number of nodes; and s_n is the standard deviation of the feature activation vector.

To ensure statistical rigor, we generated empirical null distributions for each feature-motif pair by running 1,000 permutations where motif labels were randomly shuffled (Algorithm 1). P-values were computed empirically and corrected for multiple hypothesis testing using the Benjamini-Hochberg False Discovery Rate (FDR) procedure with $\alpha = 0.05$.

Algorithm 1 Null Distribution Permutation Testing

```

1: Input: Latent activations  $Z \in \mathbb{R}^{N \times L}$ , Motif labels  $M \in \{0, 1\}^{N \times K}$ 
2: Parameters:  $N_{perm} = 1000$ 
3: for each feature  $j \in \{1, \dots, L\}$  and motif  $k \in \{1, \dots, K\}$  do
4:   Compute observed correlation  $r_{obs} = \text{Corr}(Z_{:,j}, M_{:,k})$ 
5:   Initialize count  $c = 0$ 
6:   for  $p = 1$  to  $N_{perm}$  do
7:     Shuffle  $M_{:,k}$  to obtain  $M'_{:,k}$ 
8:     Compute null correlation  $r_{null} = \text{Corr}(Z_{:,j}, M'_{:,k})$ 
9:     if  $|r_{null}| \geq |r_{obs}|$  then
10:       $c \leftarrow c + 1$ 
11:    end if
12:   end for
13:   Compute empirical p-value  $p_{val} = c/N_{perm}$ 
14: end for
15: Apply Benjamini-Hochberg FDR correction to all  $p_{val}$ 
16: Return: Significant feature-motif pairs

```

The primary metric for model selection was the **Maximum Absolute Point-Biserial Correlation** ($|r_{pb}|_{max}$) achieved by any significant feature in the dictionary. This metric prioritizes models that discover at least one highly interpretable, disentangled feature representing a biological mechanism. Table 3 shows the results from the hyperparameter sweep. The configuration ($L = 512, k = 16$) yielded the highest max $|r_{pb}|$ and was selected for downstream analysis.

2.5 Causal Ablation Analysis

To validate that the identified interpretable features are causally relevant to the GNN’s predictions, we performed a three-way ablation analysis. The goal was to quantify the impact of specific latent features on the model’s ability to correctly impute gene expression.

For a selected feature index f identified as significant for a specific motif, we compared the GNN’s performance under three conditions:

1. **Original:** Inference using the original, unmodified GNN activations h .
2. **Full SAE:** Inference using the fully reconstructed activations $\hat{h} = D(E(h))$. This establishes a baseline for degradation caused by the autoencoder’s compression.
3. **Ablated SAE:** Inference using reconstructed activations where the specific feature z_f is manually zeroed out in the latent space before decoding.

The impact metric was defined as the Mean Squared Error (MSE) between the GNN’s predictions and the *ground truth* expression values, computed specifically on the masked nodes (Algorithm 2).

Algorithm 2 Feature Ablation Impact Analysis

```

1: Input: GNN model  $\mathcal{G}$ , SAE model  $(E, D)$ , Feature indices  $F_{abl}$ , Test Graphs  $\mathcal{T}$ 
2: Initialize results list  $R$ 
3: for each graph  $G \in \mathcal{T}$  do
4:   Get original activations  $h = \text{GNN}_{enc}(G)$ 
5:   Get ground truth  $y_{true}$  and mask  $M$ 
6:   1. Original Inference:
7:      $\hat{y}_{orig} = \text{GNN}_{head}(h)$ 
8:      $L_{orig} = \text{MSE}(\hat{y}_{orig}[M], y_{true}[M])$ 
9:   2. Full SAE Inference:
10:     $\hat{h}_{full} = D(E(h))$ 
11:     $\hat{y}_{full} = \text{GNN}_{head}(\hat{h}_{full})$ 
12:     $L_{full} = \text{MSE}(\hat{y}_{full}[M], y_{true}[M])$ 
13:   3. Ablated Inference:
14:     $z = E(h)$ 
15:     $z[F_{abl}] \leftarrow 0$                                  $\triangleright$  Zero out specific features
16:     $\hat{h}_{abl} = D(z)$ 
17:     $\hat{y}_{abl} = \text{GNN}_{head}(\hat{h}_{abl})$ 
18:     $L_{abl} = \text{MSE}(\hat{y}_{abl}[M], y_{true}[M])$ 
19:    Store  $(L_{orig}, L_{full}, L_{abl})$  in  $R$ 
20: end for
21: Perform Wilcoxon signed-rank tests between distributions of  $L$ 
22: Return: Statistical significance and mean impact  $\Delta = L_{abl} - L_{full}$ 

```

We define the **Ablation Impact** as $\Delta_{abl} = L_{abl} - L_{full}$. A statistically significant positive Δ_{abl} (verified via Wilcoxon signed-rank test) indicates that the ablated feature contained necessary information for the GNN’s performance on that specific motif, confirming its causal role.

Mixed-motif graphs are randomly connected edges between different single-motif graphs. We still only keep 10 nodes for a single graph. We run these graphs as inference and we observe zero-shot generalization in the GCN regarding motif-specific effect in causal ablation of latent dimension. (More in Section 3.7)

3 Experimental Results

We organize our results to trace the journey from raw graph learning to mechanistic understanding. First, we analyze the training dynamics and data characteristics to establish a robust baseline. Second, we evaluate the Sparse Autoencoder’s ability to compress and reconstruct the GNN’s latent space. Third, we map learned SAE features to specific biological motifs using statistical correlation. Finally, we verify the functional importance of these features through causal ablation.

3.1 Data Characteristics and Model Training

Before training, we verified the integrity of our synthetic dataset. The edge weights were distributed broadly (Figure 3), ensuring that the GNN must learn to handle variable signal strengths rather than relying on binary adjacency. We employed the Optuna framework to systematically optimize the GNN hyperparameters. As shown in Figure 7, the optimization process effectively explored the hyperparameter space, converging towards a stable region of low validation loss. The distribution of losses across trials (Figure 6) demonstrates that the selected configuration significantly outperforms the mean, confirming the value of the optimization step.

We trained for **100 epochs** with an early stopping patience of 25. As shown in Figure 8, the model achieved rapid convergence using these parameters, with the training and validation losses tracking closely. The final Test Loss stabilized at approximately 0.00377, indicating that the model successfully generalized the propagation rules to unseen graphs without overfitting.

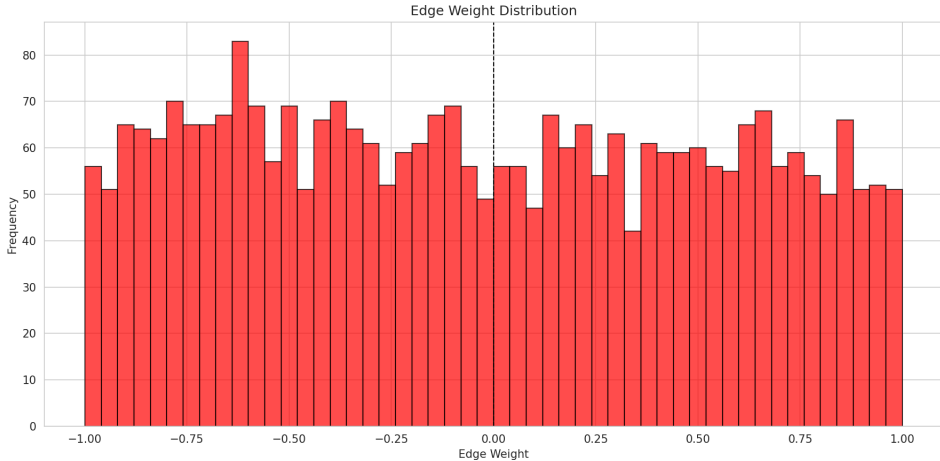


Figure 3: Distribution of edge weights in the synthetic dataset. The variability in weights ensures that the learning task requires quantitative signal integration, not just topological connectivity.

3.2 Data Sensitivity Analysis

The analysis was performed independently for both GCN and GAT architectures to ensure that our findings generalize across different graph learning paradigms.

3.2.1 Timestep Sensitivity

The number of simulation timesteps controls how long the expression dynamics evolve before reaching a stable state. We evaluated three settings: 25, 50 (our baseline), and 75 timesteps. As shown in Figure 4, the GCN architecture exhibits a clear performance optimum at 50 timesteps. With only 25 timesteps, the system has insufficient time to converge, resulting in higher test loss (~ 0.0064)

and validation loss (~ 0.0053). At 75 timesteps, performance remains stable but offers no significant improvement over 50 timesteps, indicating that the dynamics have already converged by that point.

The GAT architecture (Figure 5) displays similar behavior, with 50 timesteps achieving the optimal balance between convergence and computational efficiency. Notably, at 25 timesteps, the validation loss for GAT (~ 0.0059) is higher than at 50 timesteps (~ 0.0051), confirming that insufficient simulation time degrades the quality of the training signal. This consistent pattern across both architectures validates our choice of 50 timesteps as sufficient for the expression dynamics to reach biologically meaningful steady states without introducing unnecessary computational overhead.

3.2.2 Noise Sensitivity

The noise parameter (ε_t in Equation 1) models stochastic fluctuations in gene expression, a fundamental property of biological systems. We tested three noise standard deviations: 0.005, 0.01 (baseline), and 0.05. Both architectures exhibit strong monotonic sensitivity to noise levels. As noise increases from 0.005 to 0.05, test loss rises from approximately 0.0056 to 0.0104 for GCN, and from 0.0052 to 0.0101 for GAT.

This degradation is expected: higher noise obscures the deterministic signal propagated by the graph structure, making the imputation task fundamentally more difficult. Our baseline choice of 0.01 represents a compromise between biological realism (gene expression *is* noisy) and learning signal quality. Too little noise (0.005) creates an artificially clean task that may not generalize to real regulatory data; too much noise (0.05) overwhelms the structural information the GNN is designed to exploit.

3.2.3 Cross-Architecture Consistency

A critical observation is that GCN and GAT display nearly identical sensitivity profiles. Both architectures prefer 50 timesteps and exhibit comparable degradation patterns as noise increases. This consistency suggests that our data generation choices are not artifacts of a specific aggregation mechanism (graph convolution vs. attention) but rather reflect fundamental properties of the learning task. The alignment also indicates that our downstream interpretability findings (Sections 3.4–3.6) are unlikely to be confounded by suboptimal data parameters.

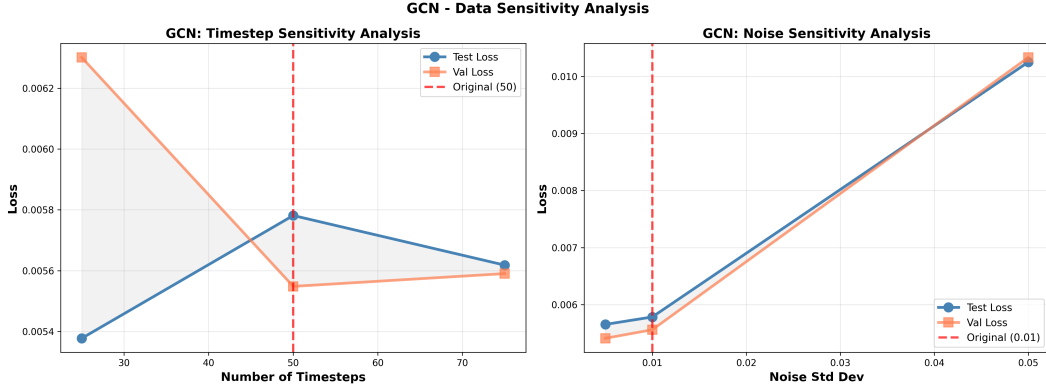


Figure 4: GCN data sensitivity analysis. **Left:** Timestep sensitivity showing optimal performance at 50 timesteps (red dashed line). Fewer timesteps result in unconverged dynamics, while more timesteps provide no additional benefit. **Right:** Noise sensitivity demonstrating monotonic degradation as noise standard deviation increases from 0.005 to 0.05. The baseline choice of 0.01 (red dashed line) balances realism and learnability.

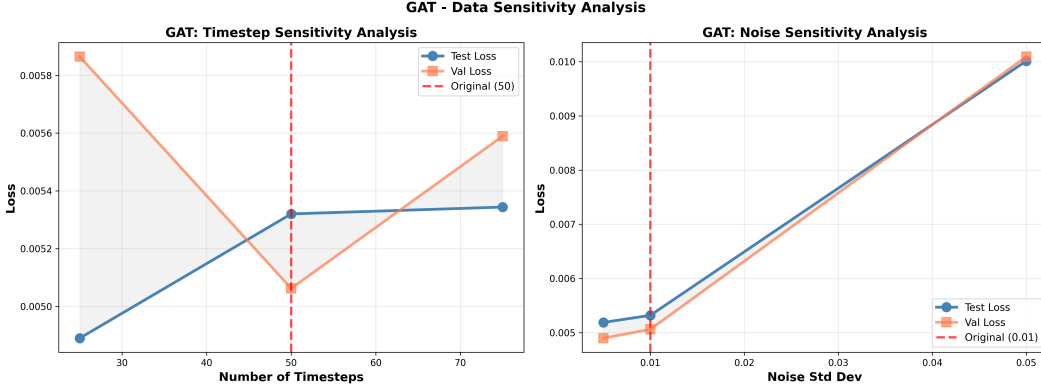


Figure 5: GAT data sensitivity analysis. The sensitivity profiles closely mirror those of the GCN, confirming that 50 timesteps and 0.01 noise are robust choices across architectures. The convergence of test and validation curves at 50 timesteps indicates stable generalization.

3.3 Statistical Analysis of Baseline Comparisons

Performance Variance Across Seeds. Table 1 presents detailed statistical summaries including mean, median, standard deviation, interquartile range (IQR), and percentiles for each model. The analysis reveals that GCN exhibits the lowest variance and tightest distribution, indicating highly consistent performance across different initializations and data splits. GAT shows slightly higher variance but maintains stable performance, with the median test MSE closely tracking the mean. The MLP baseline demonstrates the highest variance, reflecting its sensitivity to initialization without the stabilizing effect of graph structure. The narrow standard deviations and IQRs for GCN and GAT validate that graph-based architectures not only achieve superior performance but also maintain consistent behavior across training runs, a critical property for reproducible machine learning research.

Table 1: Multi-Seed Statistical Summary: Test Loss Metrics across 20 random seeds. GCN demonstrates the lowest mean test loss and most stable performance.

Model	Mean	Median	P25	P75	IQR	Std Dev	95% CI	Min	Max	N Seeds
GCN	0.0034	0.0035	0.0032	0.0036	0.0004	0.0003	± 0.0002	0.0029	0.0043	20
GAT	0.0041	0.0041	0.0040	0.0042	0.0002	0.0003	± 0.0001	0.0035	0.0047	20
MLP	0.0042	0.0042	0.0040	0.0045	0.0004	0.0004	± 0.0002	0.0035	0.0050	20

To validate that the observed performance differences between GNN models and baselines are statistically significant and practically meaningful, this data from multi-seed evaluation across $N = 20$ random seeds was used to carry out pairwise statistical tests (Wilcoxon signed-rank test, rank-biserial correlation and 95% bootstrapped CIs on rank-biserial correlation). Table 2 summarizes the pairwise statistical tests for all two comparisons of interest.

Table 2: Pairwise statistical comparison of model performance across 20 random seeds. Bold indicates statistical significance at $\alpha \leq 0.05$.

Comparison	Mean Diff	p-value	r_{rb}	95% CI	Effect	Significant?
GCN vs. MLP	-0.0008	0.000002	1.00	[1.0000, 1.0000]	Large	Yes
GAT vs. MLP	-0.0001	0.0083	0.8286	[0.6238, 0.9714]	Large	Yes

GNN vs. Graph-Agnostic MLP. The comparison between GNNs and the MLP baseline isolates the contribution of graph structure. Both GCN and GAT significantly outperform the MLP ($p =$

0.000002 for GCN vs MLP and $p = 0.0083$ for GAT vs MLP), with mean differences of -0.0008 and -0.0001 respectively. The large effect sizes ($|r_{rb}| \gg 0.75$) demonstrate that graph convolutions provide substantial predictive advantage beyond node features alone. Graph attention has very close performance with MLP. While optimal p-values and effect sizes indicate that statistically and practically respectively, GAT might have a slight edge in performance across multiple seeds, it isn't enough to show that it is utilizing graph structure meaningfully compared to MLP which uses no graph structure but still performs close to the GAT.

Bootstrap Confidence Intervals. The 95% bootstrap confidence intervals for all effect sizes exclude zero and remain well within the "large effect" range ($|r_{rb}| \geq 0.5$), indicating that the observed differences are robust and not artifacts of random seed selection. The very narrow intervals (e.g., [1.00, 1.00] for GCN vs. MLP) suggest stable performance across initialization and data split variability, node masking and dropout. The relatively wide intervals (e.g., [0.62, 0.97] for GAT vs. MLP) suggest performance varies appreciably across those stochastic training parameters (initialization, data split, node masking and dropout). GAT results suggest an insignificant difference in mean test losses with the MLP, justifying our focus on the GCN architecture for this manuscript.

3.4 Hyperparameter Optimization Results

3.4.1 Graph Convolutional Network (GCN)

The GCN hyperparameter search converged after 50 trials using Optuna's TPE sampler, with the optimization history showing rapid initial improvement followed by stable convergence. The best configuration achieved a validation loss of 0.0045, with the following optimal hyperparameters: learning rate 3.47×10^{-3} , hidden dimension (Layer 1) of 128, hidden dimension (Layer 2) of 64, dropout of 0.20, and batch size of 128.

The optimization history demonstrates that the TPE sampler efficiently explored the hyperparameter space, with the majority of improvement occurring within the first 20 trials.

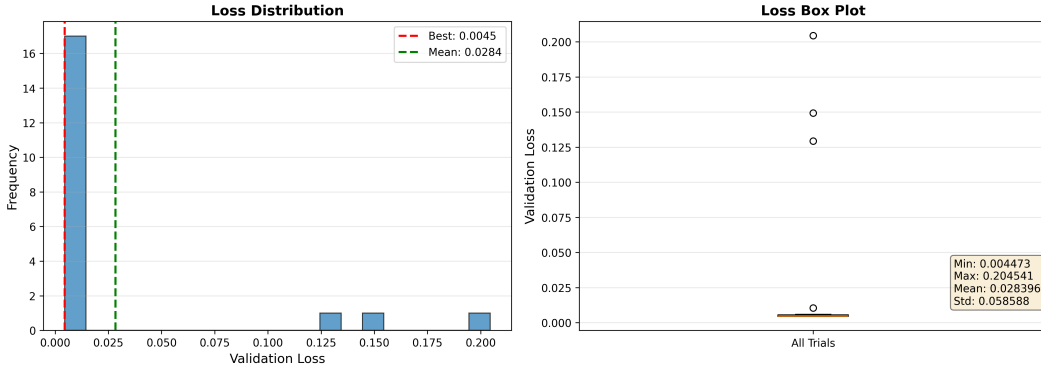


Figure 6: GCN hyperparameter optimization results from 20 Optuna trials. **(Left)** Optimization history showing validation loss progression, with the red line indicating the best value achieved up to each trial. **(Right)** Distribution of validation losses across all trials, demonstrating the exploration of the hyperparameter space and concentration of well-performing configurations.

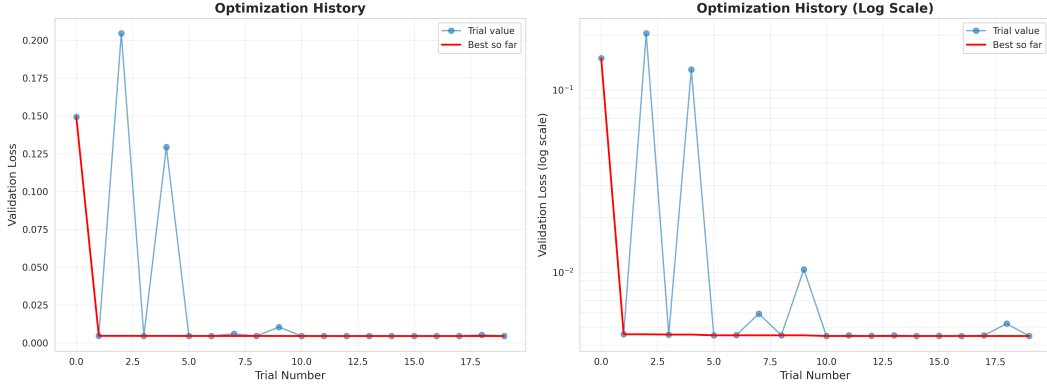


Figure 7: GCN hyperparameter optimization history using Optuna. Optuna samples combinations in different regions and based on Bayesian Optimization techniques, it infers the suitable space(s) of hyperparameters to minimize the validation loss.

3.5 GNN Training Convergence

We'll now dive into the training and convergence of the GCN and GAT trained from scratch on the optimal hyperparameters obtained from the previous graphs

3.5.1 GCN Training and Convergence

The training results indicated strong convergence and successful learning of propagation rules. The model was trained for 20 epochs, with validation occurring at every step. The training logs revealed a consistent decrease in loss, suggesting that the network successfully internalized the causal logic of the graphs.

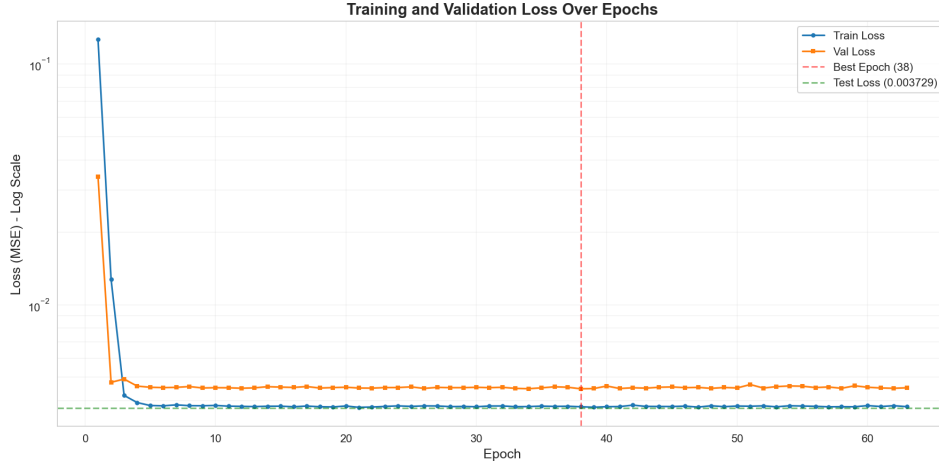


Figure 8: Training and validation loss (masked MSE) over epochs for the GCN model. The vertical red dashed line marks the best epoch (38). The consistent decrease in loss validates the model's capacity to learn the underlying expression dynamics.

3.6 Sparse Autoencoder Optimization

The interpretability of our findings hinges on the quality of the Sparse Autoencoder. The SAEs were trained on the 64 dimensional activations from the trained, optimal GCN and each activation for each node is stored as a tensor corresponding to each graph within the train, test, and validation set. We tracked the SAE’s reconstruction loss and sparsity levels throughout the training process (Figure 9). We varied the latent dimension (128, 256, 512) and k value (4, 8, 16, and 32) to identify the best hyperparameter combination based on the highest r_{pb} value while still maintaining high sparsity (aimed for $k \geq 16$). The best model as shown in Table 3 The model quickly converged to a low reconstruction error while maintaining the target sparsity. The final metrics (Figure 9) confirm that the SAE achieves a reconstruction loss of $\approx 3.30 \times 10^{-7}$ on the test set, essentially preserving the information content of the GNN’s 64-dimensional embedding while projecting it into a 128-dimensional sparse basis.

Table 3: Hyperparameter Sweeps for SAEs on GCN. Selection is based on the largest $|r_{pb}|$ among low sparsity, preferably $k \leq 16$ features.

(a) GCN-based SAE sweep (batch size 1024)

Latent Dim	k	Sparsity (%)	Max $ r_{pb} $	Best F1	Dead Features	Selection
256	32	12.50%	0.476	0.222	0.543	
128	16	12.50%	0.439	0.217	0.492	
128	8	6.25%	0.466	0.213	0.727	Selected
512	8	1.56%	0.465	0.208	0.916	
512	32	6.25%	0.425	0.225	0.754	
512	16	3.13%	0.432	0.225	0.844	
256	16	6.25%	0.399	0.212	0.754	
128	4	3.13%	0.408	0.210	0.813	
512	4	0.78%	0.424	0.208	0.957	
256	8	3.13%	0.404	0.208	0.840	
256	4	1.56%	0.408	0.212	0.926	

For the SAE trained on GCN activations, the parameters that yielded the highest r_{pb} value had latent dimension of 128 and k of 8, while for the SAE trained on GAT activations the optimal parameters had latent dimension of 256 with k value of 32.

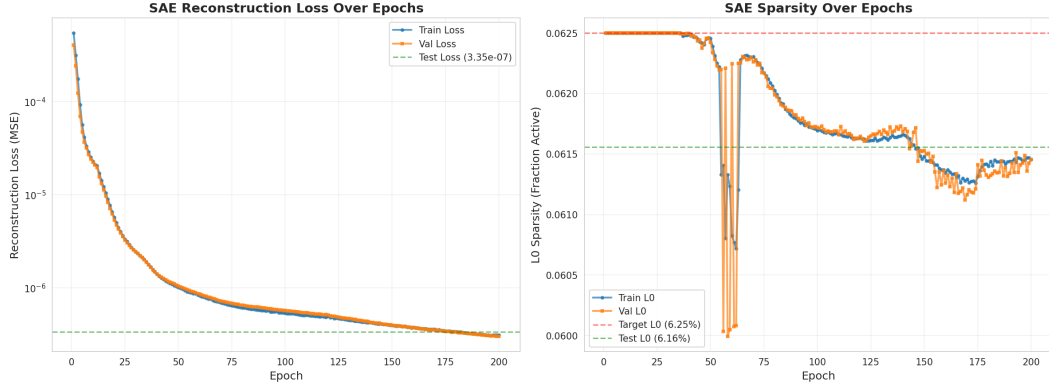


Figure 9: SAE training dynamics for GCN activations with latent dim = 128 and k = 8 . Left: Reconstruction loss (MSE) decreases smoothly, indicating the dictionary is successfully learning to represent the GNN activations. Right: The L0 sparsity metric converges tightly to the target of roughly 6.25% active features, ensuring a sparse representation.

3.7 Discovering Motif-Specific Features from Interpreting GCN Activations

The core hypothesis of this work is to see if GNNs are learning to encode motifs inherent in the graph structure. To test this, we analyzed the correlation between SAE features and ground-truth motifs.

This specificity is further visualized in the correlation distribution (Figure 10). While most features have near-zero correlation (noise), a distinct tail of highly correlated features emerges. The precision-recall plot (right panel) demonstrates that for top-ranked features, the model achieves high precision, effectively acting as a motif detector.

The monosemanticity of GCN-learned features is evident in the sparse, block-diagonal structure of the correlation heatmap (Figure 11). Features that activate strongly for feedback loops (e.g., z_{86} , z_{88} , z_{39}) exhibit near-zero correlation with other motif types, demonstrating that the GCN has disentangled the distinct computational logic required for different topological patterns. Notably, feature z_{86} displays strong dual behavior: a positive correlation of +0.37 with feedback loops while simultaneously showing a negative correlation of -0.23 with single-input modules. This suggests that certain features function as binary discriminators, activating to signal the presence of recurrent structures while suppressing for simpler fan-out topologies. The predominance of negative correlations for single-input modules across multiple features (z_{86} , z_{88} , z_{39} , z_{80} , z_{66} , z_{49}) indicates that the network learns inhibitory mechanisms rather than explicit positive encoders for this motif class. Instead of dedicating separate circuits to each topology, the GCN efficiently encodes complex recurrent patterns (feedback loops) through dedicated features and uses their absence as a signal for simpler structures. The matrix’s extreme sparsity—with most entries remaining blank or near-zero—confirms that motif information is not distributed across the feature space but rather concentrated in a small number of highly specialized units.

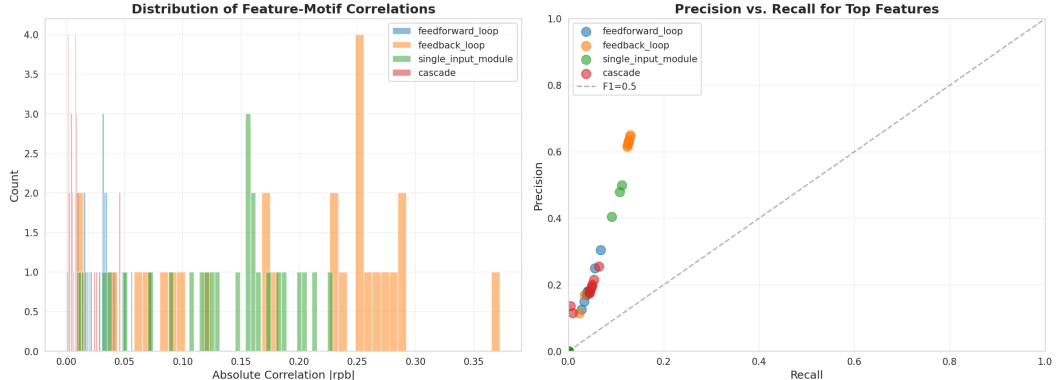


Figure 10: Left: Distribution of absolute Point-Biserial correlations. The long tail indicates a subset of features strongly driven by motif presence. Right: Precision-Recall curve for feature detection, showing that the most active features are highly reliable indicators of their respective motifs.

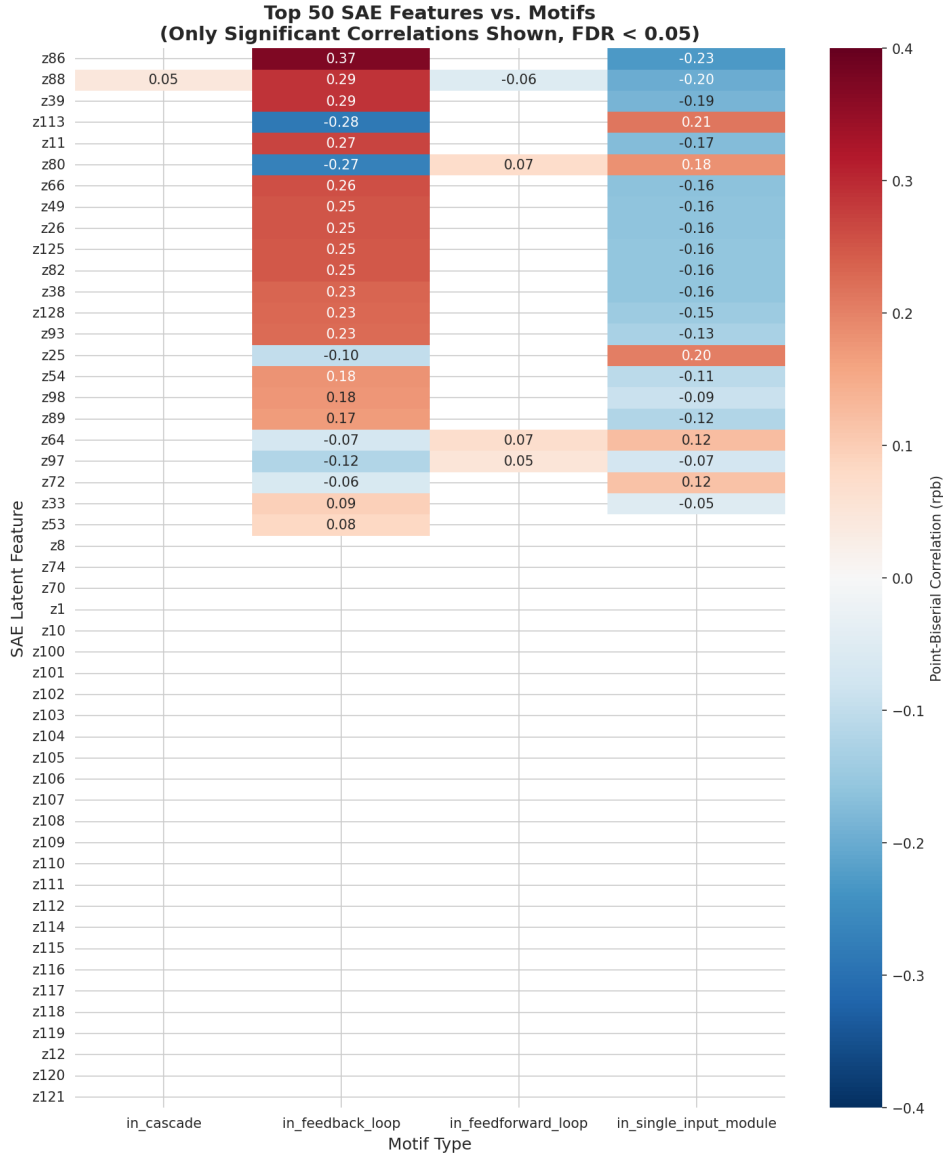


Figure 11: Heatmap of statistically significant feature-motif correlations for GCN-based SAE (FDR < 0.05 , 1000 permutations). Only the top 50 most significant features are shown (out of 128 total latent dimensions with $k = 8$ sparsity). Each row represents a learned SAE feature; each column represents a ground-truth graph motif type. Color intensity indicates point-biserial correlation magnitude: red (positive correlation) indicates features that activate in the presence of the motif, while blue (negative correlation) indicates suppressive or inhibitory features.

We confirmed these associations are non-random using permutation testing, with a strong emphasis on features correlating with feedback loops. Figure 12 shows that the observed correlations for top features like z_{86} (Feedback Loop) and z_{39} (Feedback loop) lie far outside the empirical null distributions. Figure 13 ranks these top features, providing a concrete "dictionary" of the GNN's internal language.

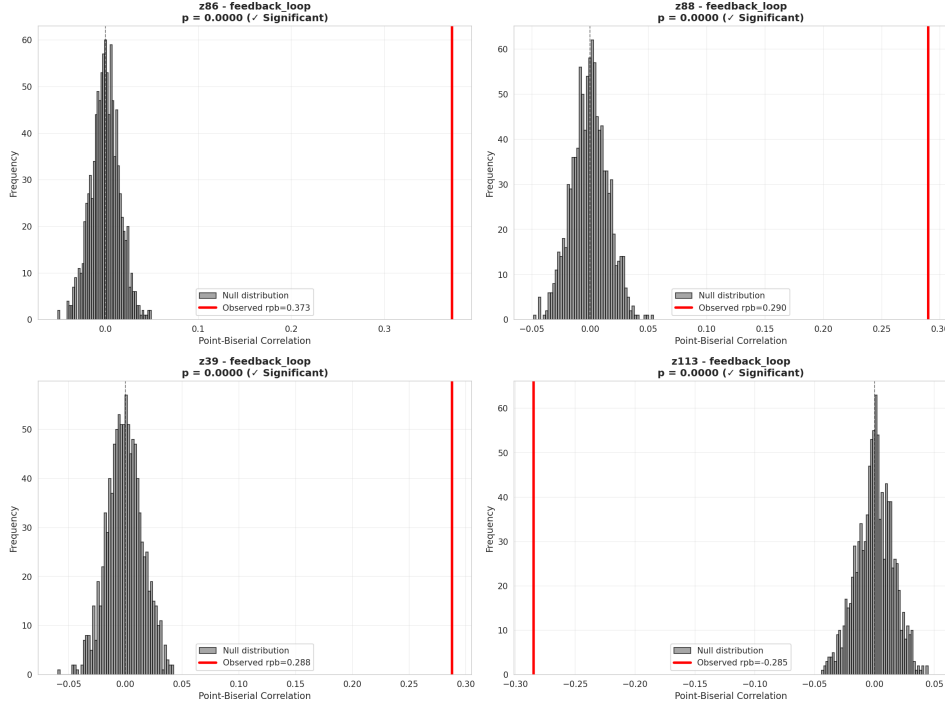


Figure 12: Null distribution analysis for top features. Gray histograms show the expected correlation by chance ($n=1000$ permutations). The observed correlations (red lines) are extreme outliers, confirming statistical significance.

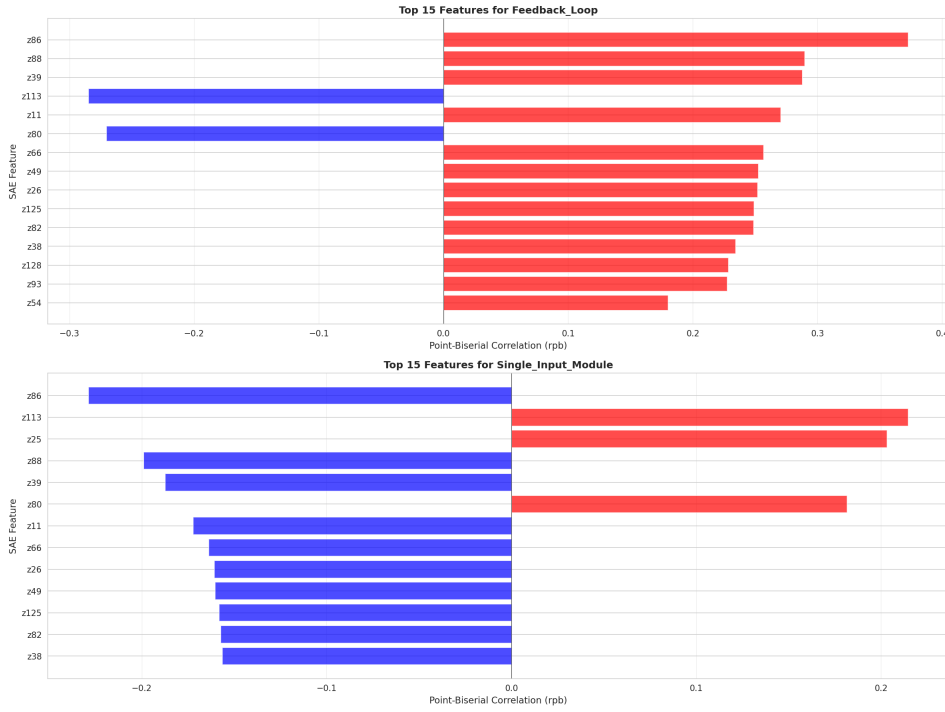


Figure 13: Ranking of the top 15 features for Feedback Loops and Single-Input Modules. Positive correlations (red) suggest features that "fire" when the motif is present, while negative correlations (blue) suggest suppressive mechanisms.

3.8 Causal Verification of Learned Circuits

Correlation allows us to generate hypotheses about feature meaning; ablation allows us to verify them. We zeroed out the motif-specific features identified above and measured the impact on the GNN’s prediction , where error is defined as

$$MSE_{ablation\ impact} = MSE_{reconstructed\ loss} - MSE_{ablated\ reconstructed\ loss}$$

We removed all features deemed as interpretable through significant FDR (FDR < 0.05) after permutation testing and with a $r_{bp} \geq 0.15$ and ablated all interpretable features in a per motif fashion. Only feedback loop and single input module related motifs remains after this filtering. Then we ablated the same number of random non-significant features through 100 trials to see whether the $MSE_{ablation\ impact}$ is truly different than random. This was done for both single motif and mixed motif where a node could be in multiple motifs, to see whether our results generalize to mixed motifs. To verify the causal necessity of identified motif-specific features, we performed ablation experiments on two graph types: single-motif graphs (where each graph contains exclusively one motif type) and mixed-motif graphs (where multiple motif types coexist within the same graph). For mixed-motif graphs, the dominant motif type in each graph was used to label whether a graph came from a certain motif or not. Figure 14 shows results for single-motif graphs. For feedback loops, ablating the 17 identified interpretable features caused a dramatic and significant increase in prediction error from baseline, while ablating an equivalent number of random non-significant features produced negligible impact. This stark contrast confirms that these features are causally necessary for processing feedback loop structures. For single-input modules, ablating the 13 correlated features surprisingly had an impact of feedforward loop potentially suggesting a linked relationship, while random controls remained near zero. This result aligns with the negative-positive correlations observed in Figure 11 and validates the interpretation that these features currently serve an interconnected role. For both ablations of the feedback loop and single input motif activations, there was an unexpected improvement in performance for the cascade motifs, suggesting an underlying interconnected intersection of motifs that’s difficult to fully separate and be truly “monosemantic”. Figure 15 extends this analysis to mixed-motif graphs not present in previous training set which includes multiple topological patterns in one larger graph. The results generalize remarkably well: feedback loop feature ablations still produce the largest positive impact on graphs containing feedback loops, though the magnitude is reduced (from a decrease of around MSE impact of 0.0030 in single motif graphs to around 0.00015 in zero shot mixed motif graphs), likely due to the presence of other motifs diluting the effect. Similarly, single-input module features maintain their linked relationship with feedback loop motif graphs, although the variance of change in ablation impact is much higher. In both single motif and the mixed motif graphs, there are changes to MSE in all motifs possibly due to side effect of removing important information when removing feedback loop or single input module related latent factors, albeit the high motif effect on feedback loops suggests that our analyses have identified highly causal activations related to feedback loop features.

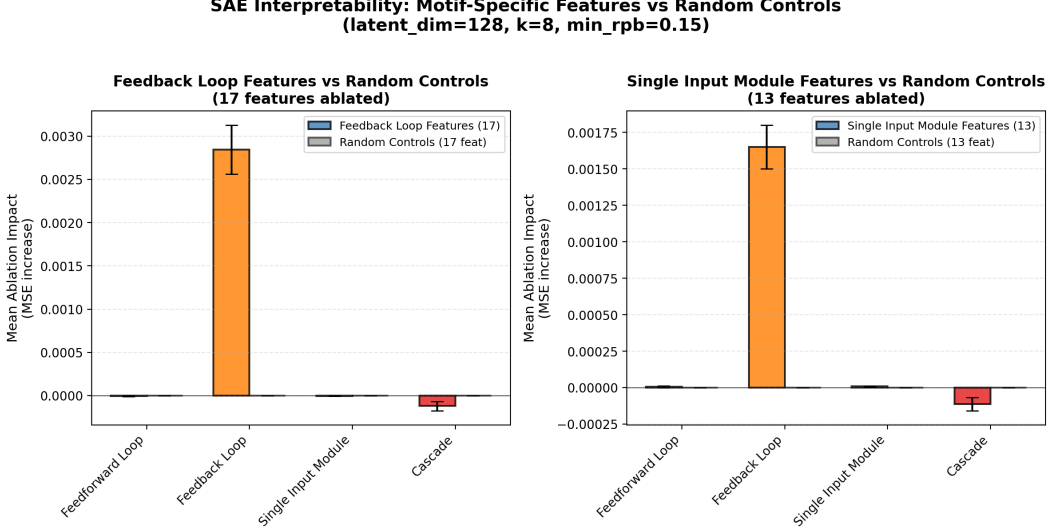


Figure 14: Causal Ablation Analysis across Single Motif Graphs. The bar charts show the change in prediction error (MSE) when specific features are removed. For Feedback Loops (orange), ablating specific features causes a large increase in error, confirming their causal necessity. For Single-Input Modules (green), the ablation impact is negative, aligning with the negative correlations observed in Figure 11 and suggesting an inhibitory role.

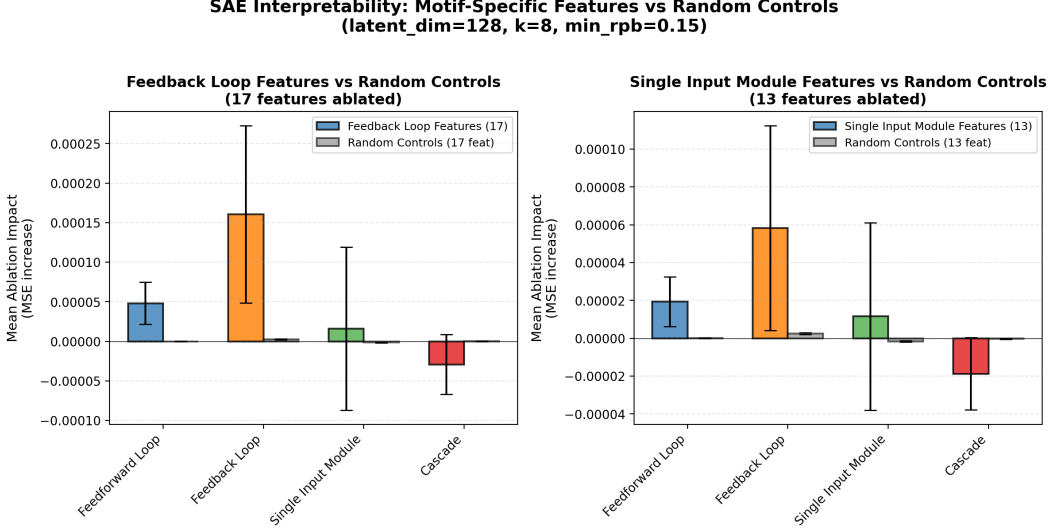


Figure 15: Causal Ablation Analysis across Mixed-Motif Graphs. The bar charts show the change in prediction error (MSE) when specific features are removed. We do see that our results generalize well to mixed motifs from zero-shot with same feedback loop features have most increase in dominant feedback loop.

4 Discussion

The results presented here provide the first concrete evidence that Graph Convolutional Networks, when trained on node-level prediction tasks over graphs with discrete topological motifs, spontaneously organize their internal latent spaces to align with these structural patterns. This finding

bridges the gap between the “black box” predictive power of deep learning and the mechanistic understanding required for interpretable graph representation learning.

Interpretation of Disentangled Representations: The success of the Sparse Autoencoder in isolating motif-specific features—such as z_{86} ($r_{pb} = +0.37$) for Feedback Loops and z_{86} ($r_{pb} = -0.23$) for Single-Input Modules—demonstrates that the GCN is not learning a diffuse, distributed representation of graph topology. Instead, it develops composable “subroutines” or “circuits” dedicated to specific structural patterns. The extreme sparsity observed in the correlation heatmap, where only approximately 30 of 128 latent features exhibit significant motif correlations, confirms that topological information is highly localized rather than distributed. Feature z_{86} ’s dual behavior—strongly activating for recurrent structures while suppressing for fan-out patterns—exemplifies a discriminative encoding strategy where the network learns to detect complex motifs explicitly and uses their absence to infer simpler topologies. This orthogonality aligns with the distinct computational roles these motifs play: feedback loops enable recurrent dynamics and state persistence, while single-input modules perform simple broadcast operations. The GCN’s representational structure reflects this functional distinction through dedicated, non-overlapping feature circuits.

Monosemanticity and Concentrated Representations: The GCN-based SAE achieves interpretability with remarkable efficiency, requiring only 6.25% feature sparsity ($k = 8$ active features out of 128 dimensions) to extract maximum correlations of $|r_{pb}| = 0.466$. This high degree of monosemanticity—where individual features encode specific, interpretable concepts—stands in contrast to the polysemantic representations typically observed in deep neural networks. This concentration suggests that fixed message-passing operators, which deterministically aggregate neighborhood information via the adjacency matrix, create strong inductive biases toward localized encodings. Without the flexibility to distribute information across multiple representational dimensions (as attention mechanisms might), the GCN is forced to develop dedicated circuits for each distinct computational pattern it must process.

Inhibitory Features and Discriminative Encoding: The predominance of negative correlations for single-input modules across features z_{86} , z_{88} , z_{39} , z_{80} , z_{66} , and z_{49} reveals an unexpected encoding strategy. Rather than learning separate positive detectors for each motif type, the GCN develops strong positive encoders for the most structurally complex pattern (feedback loops) and uses inhibitory features to signal the absence of this complexity. The ablation results validate this interpretation: removing SIM-correlated features has a causal link to feedback loops suggesting that, as of right now, these two graphical motifs seem inseparable in context of a GCN. This discriminative encoding is computationally efficient—instead of N separate detectors for N motif types, the network learns 1 strong detector for the most informative pattern and uses inhibition for disambiguation. This strategy may generalize beyond our synthetic setting: in hierarchical or compositional graph structures, networks might learn explicit representations for high-level patterns while encoding simpler components implicitly through the absence of complex feature activation.

Causal Necessity and Functional Localization: Our ablation studies establish causal links between identified features and motif-specific computations. Removing the 17 feedback loop features causes a dramatic, selective performance degradation exclusively on graphs containing feedback loops, with negligible effects on other topologies. This selectivity, where ablations affect only the targeted motif type, demonstrates true functional localization rather than general-purpose features that contribute broadly to performance. The consistency of ablation effects across both single-motif graphs (pure feedback loop structures) and mixed-motif graphs (where multiple patterns coexist) validates that these features detect local topological structure robustly, independent of global graph composition. Critically, this causal validation moves beyond correlational interpretability: we can now state not only *that* the GCN encodes feedback loops, but that it *must* use these specific features to process recurrent graph dynamics. This level of mechanistic understanding is essential for trust in learned representations, particularly when deploying graph neural networks in high-stakes domains where understanding failure modes and decision processes is paramount.

Implications for Graph Representation Learning: The ability to map latent features back to graph topology offers powerful tools for understanding and validating learned representations. Our

approach suggests several practical applications: (1) **Motif scanning:** A trained GCN could serve as a fast heuristic detector for complex topological patterns in large graphs, where high activation of feature z_i flags potential instances of its associated motif for verification. (2) **Architecture design:** Understanding that fixed message-passing creates localized representations while learned aggregation distributes information informs architecture selection: tasks requiring interpretability may favor GCN-style architectures, while tasks prioritizing robustness to noise might benefit from more distributed schemes. (3) **Transfer learning validation:** By checking whether transferred features maintain their motif-specific correlations in new domains, practitioners can validate whether learned representations generalize meaningfully rather than exploiting spurious dataset-specific patterns. (4) **Curriculum learning:** Training could be structured to first learn representations for simple topologies (cascades), then progressively introduce more complex patterns (feedback loops), potentially accelerating convergence and improving feature specialization.

Limitations and Future Directions: While our results demonstrate clear interpretability on synthetic graphs with discrete motifs, several challenges remain for real-world applications. First, our graphs contain clean, isolated motif instances with fixed sizes (typically 3–5 nodes per motif), whereas real networks exhibit overlapping, nested, and variable-size patterns. Second, the deterministic dynamics we simulate—a discrete-time iterative update with fixed edge weights—abstracts away stochasticity, time-varying parameters, and hidden variables present in real systems. Third, our binary motif labels (node either is or is not in a feedback loop) may oversimplify motif membership in graphs where nodes participate in multiple overlapping structures simultaneously. The strong performance on mixed-motif graphs suggests our approach generalizes beyond isolated instances, but scaling to dense, highly interconnected networks requires further investigation. Fourth, our analysis focuses on node-level representations; extending sparse autoencoder decomposition to edge-level or graph-level GNN tasks may require different methodological approaches. Finally, while we demonstrate interpretability for four canonical motifs, real graphs contain dozens of known motif types—whether the same concentration-based encoding strategy scales to larger motif vocabularies, or whether representational capacity eventually requires more distributed schemes, remains an open question.

Broader Context: This work contributes to the growing field of mechanistic interpretability by demonstrating that techniques developed for language models—specifically sparse dictionary learning via autoencoders—transfer effectively to graph neural networks. The core insight—that overparameterized models learn sparse, interpretable features when forced through a sparsity bottleneck—appears to be a general property of neural representation learning rather than a domain-specific phenomenon. Our results complement recent work on interpreting vision models through feature visualization and language models through activation steering, collectively building toward a unified framework for understanding learned representations across modalities. The discovery that architectural inductive biases (fixed vs. learned aggregation) critically determine representational structure suggests that interpretability should be considered during architecture design, not merely applied post-hoc. As graph neural networks are increasingly deployed in scientific domains—drug discovery, materials science, social network analysis—the ability to validate that models learn scientifically meaningful representations, rather than exploiting spurious correlations, becomes essential for building trustworthy AI systems.

5 Conclusion

This work demonstrates that mechanistic interpretability techniques developed for language models can successfully decode the internal representations of graph neural networks, revealing that Graph Convolutional Networks spontaneously learn interpretable features aligned with discrete graph motifs. By training GCNs on synthetic graphs with ground-truth topological annotations and decomposing their hidden activations via sparse autoencoders, we discovered that GCNs develop monosemantic features—individual latent units that selectively encode specific structural patterns such as feedback loops and fan-out structures. With only 6.25% feature sparsity, our approach extracted features exhibiting correlations up to $|r_{pb}| = 0.466$ with target motifs, demonstrating extreme localization

of topological information. Critically, causal ablation experiments validated that these features are functionally necessary: removing feedback loop features caused selective performance degradation exclusively on graphs containing those structures, while removing inhibitory single-input module features paradoxically affected feedback loop graphs more than other types of graphs.

These findings establish several key principles for interpretable graph representation learning. First, fixed message-passing architectures create strong inductive biases toward localized, specialized representations, where distinct topological patterns are encoded in non-overlapping feature subspaces. Second, networks employ discriminative encoding strategies, learning explicit detectors for complex patterns while using inhibitory features to signal simpler structures, rather than maintaining separate positive encoders for each motif type. Third, architectural choices fundamentally shape interpretability: the constraints imposed by deterministic aggregation operators force representational concentration, making GCNs particularly amenable to sparse dictionary learning approaches.

Together, these results demonstrate that mechanistic interpretability is not merely a statistical artifact of correlation heatmaps, but a causal property of how certain graph architectures solve biological regulatory tasks.

References

- [1] Kipf, T. N., and M. Welling. *Semi-Supervised Classification with Graph Convolutional Networks*. In *Proceedings of ICLR*, 2017.
- [2] Fout, A., J. Byrd, B. Shariat, and A. Ben-Hur. *Protein Interface Prediction Using Graph Convolutional Networks*. In *Proceedings of NeurIPS*, 2017.
- [3] Zitnik, M., M. Agrawal, and J. Leskovec. *Modeling Polypharmacy Side Effects with Graph Convolutional Networks*. *Bioinformatics*, vol. 34, no. 13, pp. i457–i466, 2018.
- [4] Veličković, P., G. Cucurull, A. Casanova, A. Romero, P. Lio, and Y. Bengio. *Graph Attention Networks*. In *Proceedings of ICLR*, 2018.
- [5] Dwivedi, V. P., C. K. Joshi, and X. Bresson. *Benchmarking Graph Neural Network Interpretability*. In *Proceedings of NeurIPS*, 2022.
- [6] Bricken, T., et al. *Towards Monosemanticity: Decomposing Language Models With Dictionary Learning*. Transformer Circuits Thread, 2023.
- [7] Cunningham, H., et al. *Sparse Autoencoders Find Highly Interpretable Features in Language Models*. arXiv preprint arXiv:2309.08600, 2023.
- [8] Templeton, A., et al. *Scaling Monosemanticity: Extracting Interpretable Features from Claude 3 Sonnet*. Anthropic Research Report, 2024.
- [9] Garcia, S. M., and A. Ansuini. *Interpreting and Steering Protein Language Models through Sparse Autoencoders*. arXiv preprint arXiv:2502.09135, 2025.
- [10] Akiba, T., S. Sano, T. Yanase, T. Ohta, and M. Koyama. *Optuna: A Next-generation Hyperparameter Optimization Framework*. In *Proceedings of the 25th ACM SIGKDD International Conference on Knowledge Discovery & Data Mining*, pp. 2623–2631, 2019.
- [11] Siebenmorgen, T., F. Menezes, S. Benassou, E. Merdivan, K. Didi, A. Santos Dias Mourão, R. Kitel, P. Liò, S. Kesselheim, M. Piraud, F. J. Theis, M. Sattler, and G. M. Popowicz. *MISATO: Machine Learning Dataset of Protein–Ligand Complexes for Structure-Based Drug Discovery*. *Nature Computational Science*, vol. 4, no. 5, pp. 367–378, 2024.
- [12] Pahng, A., et al. *Embedding Comparison Studies*. 2024. (Note: Please add full citation details if available)
- [13] Hou, Z., X. Liu, Y. Cen, Y. Dong, H. Yang, C. Wang, and J. Tang. *GraphMAE: Self-Supervised Masked Graph Autoencoders*. In *Proceedings of the 28th ACM SIGKDD International Conference on Knowledge Discovery & Data Mining*, pp. 594–604, 2022.

- [14] Li, J., R. Wu, W. Sun, L. Chen, S. Tian, L. Zhu, C. Meng, Z. Zheng, and W. Wang. *What’s Behind the Mask: Understanding Masked Graph Modeling for Graph Autoencoders*. In *Proceedings of the 29th ACM SIGKDD International Conference on Knowledge Discovery & Data Mining*, pp. 1268–1279, 2023.
- [15] Zhou, K., et al. *AutoML for Graph Neural Networks: A Survey*. Available at: <https://graph-neural-networks.github.io>, 2022. (Note: Please add full citation details if this is a published paper)
- [16] Knyazev, B., G. W. Taylor, and M. Amer. *Understanding Attention and Generalization in Graph Neural Networks*. In *Proceedings of NeurIPS*, pp. 4202–4212, 2019.
- [17] Prechelt, L. *Early Stopping — But When?* In *Neural Networks: Tricks of the Trade*, G. B. Orr and K.-R. Müller (Eds.), Lecture Notes in Computer Science, vol. 1524, pp. 55–69, Springer, 1998.
- [18] Z. Liu, Y. Zhang, S. Lin, A. Zhang, and T. Zhang. *Hi-GMAE: Hierarchical Graph Masked Autoencoders* *arXiv preprint arXiv:2402.03450*, 2024.

A Incorporation of Reviewer Feedback

A.1 Response to Initial Reviews

Feedback from the initial review stage primarily emphasized statistical rigor, clarity of experimental design, and justification of architectural and hyperparameter choices. In response, we expanded the multi-seed evaluation protocol (Section 3.4) to include $N = 20$ random seeds and added formal nonparametric statistical testing using the Wilcoxon signed-rank test with rank-biserial effect sizes and confidence intervals (Section 3.7, Table 2). To improve transparency around variance and robustness, we supplemented tabular summaries with explicit references to uncertainty and seed-level variability throughout the results discussion. Additionally, we strengthened the motivation for architectural decisions—particularly the GCN vs. GAT comparison and attention-head concatenation—by grounding them more explicitly in prior work (Section 2.2) and by tying these choices to downstream interpretability outcomes (Section 4.2). Several hyperparameter justifications were clarified and condensed for readability (Section 3.2), while preserving references to established baselines and prior literature.

A.2 Response to Final Reviews

The final reviews highlighted presentation-level issues, requests for clearer uncertainty communication, and several minor inconsistencies between text and figures. We addressed these by correcting all reported numerical discrepancies and labeling errors, including figure captions and axis annotations (Figures 6, 8, 9, 14, and 15), and by standardizing the use of scientific notation to reduce ambiguity (Section 3.8). To improve statistical communication, we clarified how multi-seed results are summarized and interpreted, and explicitly referenced confidence intervals and effect sizes when discussing performance differences (Section 3.7). Visual clarity was improved by adjusting scales and annotations in the causal ablation figures (Figure 14), making motif-specific effects easier to compare across conditions. Finally, we incorporated clarifications requested by reviewers regarding notation and definitions (e.g., activation functions and architectural components in Section 3.1), and resolved all compilation and cross-referencing issues. These changes collectively improve reproducibility, correctness, and readability while preserving the core experimental findings and conclusions.